remote sensing

MDPI

Article

Dynamic Field Retrieval and Analysis of Structural Evolution in Offshore Core Area of Typhoon Higos Based on Ground-Based Radar Observation

Ruiyi Li [1,2,3], Qifeng Lu [1,2,4,*], Ming Wei [5], Lei Wu [3], Ruifeng Li [6], Shudong Wang [7] and Hua Liu [8]

1 Chinese Academy of Meteorological Sciences, Beijing 100081, China
2 University of Chinese Academy of Sciences, Beijing 100049, China
3 CMA Meteorological Observation Centre, Beijing 100081, China
4 CMA Earth System Modeling and Prediction Centre, Beijing 100081, China
5 School of Atmospheric Physics, Nanjing University of Information Science and Technology, Nanjing 210044, China
6 Shuozhou Meteorological Office of Shanxi Province, Shuozhou 036000, China
7 CMA Public Meteorological Service Center, Beijing 100081, China
8 CMA Meteorological Training Centre, Beijing 100081, China
* Correspondence: luqf@cma.gov.cn; Tel.: +86-10-6840-940

Abstract: Three ground-based radars in the Pearl River Delta successfully observed Typhoon Higos (2020), which traveled over the offshore area in the South China Sea. During the observation period, the stratiform region of the outer rainband of HIGOS became active while swirling inward, merging into an unclosed eyewall and spreading outward, but its structure was asymmetric between upwind and downwind. To understand the dynamic mechanism of the asymmetry of the stratiform region in detail, the refined wind speed distributions in the inner core of Higos was retrieved by using the radar observation data and a three-dimensional, variational, direct, data assimilation, Dual-Doppler analysis (DDA). In addition, an Observing System Simulation Experiment (OSSE) was conducted with the numerical simulations by the Weather Research and Forecasting (WRF) model and numerical emulations by Cloud Resolving Model Radar SIMulator (CR-SIM) software to validate the retrieved data. From the OSSE, the emulated retrieved data were comparable with the WRF-out data. The analysis shows that the dynamic mechanisms are different between upwind and downwind in the stratiform rainband. In the former, the inflow sinks in the middle troposphere. In addition, there is an inflow in the lower troposphere, with an outflow aloft the inflow. In the latter, however, the stratiform rainband is primarily influenced by outflow from inside the rainband and inflow from outside the monsoon-related southwesterly winds. The vertical velocity characteristics in the stratiform rainband downwind also differ from those upwind. The upwind updraft was distinct in the middle troposphere, whereas the downwind updraft was caused by the convergence of the outflow from inside the stratiform rainband and the monsoon-related southwesterly inflow in the lower troposphere.

Keywords: ground-based radar; wind retrieval; stratiform rainband; Typhoon Higos

check for updates

Citation: Li, R.; Lu, Q.; Wei, M.; Wu, L.; Li, R.; Wang, S.; Liu, H. Dynamic Field Retrieval and Analysis of Structural Evolution in Offshore Core Area of Typhoon Higos Based on Ground-Based Radar Observation. *Remote Sens.* **2023**, *15*, 809. https://doi.org/10.3390/rs15030809

Academic Editors: Haonan Chen and Haoran Li

Received: 25 December 2022
Revised: 27 January 2023
Accepted: 27 January 2023
Published: 31 January 2023

Copyright: © 2023 by the authors. Licensee MDPI, Basel, Switzerland. This article is an open access article distributed under the terms and conditions of the Creative Commons Attribution (CC BY) license (https://creativecommons.org/licenses/by/4.0/).

1. Introduction

The structural evolution of the TC inner core, such as the eyewall and spiral rainband, are important to the intensity of TCs [1–4]. TC rainbands (TCRs) are located outside the eyewall, affecting the development of the eyewall, which attracted the attentions of scientists for years. Generally, two types of TCRs are defined based on their positions and movements relative to the storm center: inner and outer rainbands. Inner rainbands are typically located near the eyewall, and outer rainbands usually develop farther outside the eyewall, ≥150 km from the center [5–7].

Observation showed that there were discrete or connected convective cells in the upwind of the circulation in the TCRs, but stratiform precipitation in the downwind of the circulation [1,2,8,9]. The upwind convective precipitation and downwind stratiform precipitation of TCRs are mainly affected by the environment vertical wind shear [5,9–12] (VWS). The ice particles generated by the convective cells move towards downwind with the circulation, melting and forming a wide range of stratiform precipitation, which mainly occurs in the left side of VWS [13]. According to researchers' findings, the stratiform sectors of TCRs are much closer to the typhoon eyewall, so they can impact the overall dynamics of the typhoon more directly [10,14–18]. The stratiform has weak vertical velocity, which develops upward in the middle and upper troposphere of the TCRs, but downward in the lower troposphere. Qiu et al. [4] discovered that sinking inflow exits in the middle troposphere of the stratiform sector of the outer rainband. Didlake et al. [19,20] considered that the mid-level sinking inflow in the outer rainband is associated with the melting of ice particles and the evaporation of liquid water, and the tangential wind speed jet generated at the convergence of the sinking inflow induces the typhoon intensity to increase. These phenomena indicate that, despite the weakness of the vertical velocity in the stratiform sector of TCRs, it still has obvious dynamic characteristics and plays an obvious role in the change of typhoon intensity, so more detailed observation is needed to understand its mechanism.

However, observations of the fine structure in the inner core of typhoons over the ocean are not easy to obtain. At present, advanced airborne radar is the main observation equipment to detect the fine structure of typhoons on the far ocean surface. By studying the typhoon data observed by airborne radar, scholars have gained an in-depth understanding of the structural evolution of the TCRs. When typhoons are offshore, coastal ground-based radar can observe them. Cha et al. [21] believed that coastal ground-based radar with high spatial-temporal resolution can continuously observe the structural changes of offshore typhoons for a long time, which is an advantage of ground-based radar observation. Yet, because ground-based radars are limited by their covered range, they always output the dual-Doppler wind analysis poorly, as the airborne radars do, failing to obtain the fine dynamic field of the inner-core structures of typhoons. Many scholars have tried to use ground-based single radar to retrieve typhoon wind fields offshore. Wen-Chau Lee [22] first proposed the Ground-Based Radar Velocity Tracking Display (GBVTD) method, by which the horizontal wind of the typhoon vortex can be obtained based on the radial velocity retrieval of a single radar, under the assumption that the typhoon vortex is approximately symmetric. Jou [23] redefined the radial wind according to the spacing of the radial wind relative to the typhoon center observed by radar, improving the GBVTD technology and forming the generalized velocity tracking display (GVTD) method. However, Cha [24] analyzed that the GVTD method was still affected by the lack of tangential wind, which could produce obvious retrieval errors in the asymmetric structural sectors of typhoon. Zhou Shenghui and Wei Ming [25,26] optimized the single-Doppler radar volume velocity processing (VVP) method, using it to retrieve the vertical velocity in the central area of super typhoon Saomai, but this method still has its limitation if the wind field in a certain volume is not uniform or linear.

In 2020, Typhoon Higos made landfall in Jinwan District, Zhuhai City, China. After moving to the offshore area, the typhoon developed from an obvious asymmetric structure to a symmetrical structure, and the stratiform sector of outer rainband was active, especially the downwind of stratiform, which is different from the upwind. The active evolution of stratiform was successfully observed by the densely distributed three ground-based radars in the Pearl River Delta. In this paper, we intend to construct a dual-Doppler wind analysis based on the radar observations and acquire the fine dynamic field in the inner-core area of the typhoon, and we will analyze the dynamic characteristics of the stratiform of the outer rainband of Typhoon Higos to understand the asymmetrical mechanism between the upwind and downwind in detail. The structure of this paper is arranged as follows. Section 2 introduces Typhoon Higos and related radar observation, and in Section 3 is the

wind field retrieval method and reliability verification of vertical velocity of the retrieval method. Section 4 analyzes the dynamic features of the stratiform sector of the outer rainband, and finally, Section 5 delivers the summary and conclusions.

2. Materials

According to China Meteorological Administration (CMA) best track data (Figure 1), after the genesis of Higos at 12:00 UTC on 16 August 2020 from the eastern Philippines, Typhoon Higos moved west–northwestward over the South China Sea, where sea surface temperatures (SSTs) were over 29 °C while intensifying. The maximum wind of 35 m/s occurred at 21:00 UTC on 18 August, with central pressure 970 hPa. Typhoon Higos made landfall at 22:00 UTC on 18 August, then the intensity rapidly decreased. The vector arrows in Figure 1b represent the VWS vector of 200–850 hPa, which shows that the speed of VWS is small and the direction is mainly northwest.

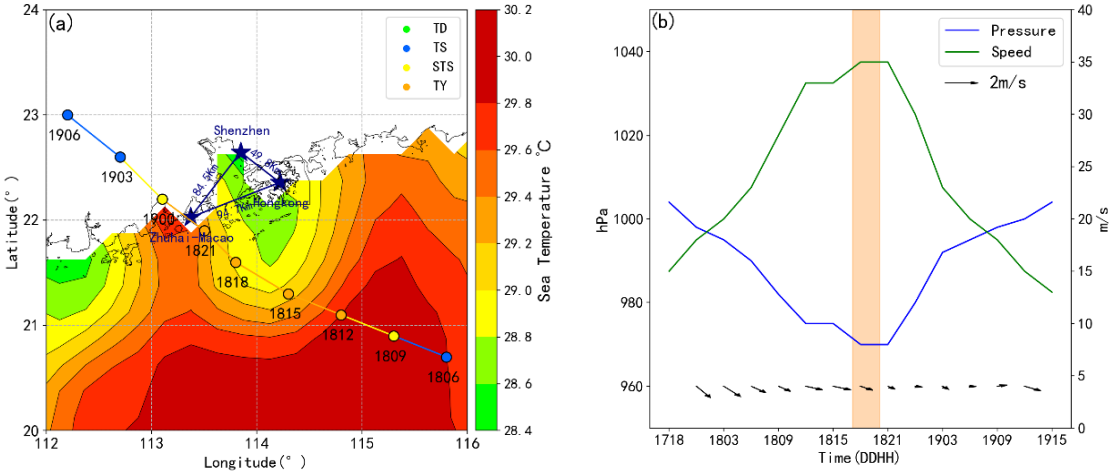

Figure 1. (**a**) The best track of Typhoon Higos and the sea surface temperature (SST) on 18 August 2020. The circled dots show 3 h intervals along the track. The dark blue asterisks denote the locations of the three radars. The SST data are from the Optimum Interpolation Sea Surface Temperature (OISST) Dataset of the National Oceanic and Atmospheric administration (NOAA) National Climatic Data Center (NCDC). The best track data are from the CMA website https://tcdata.typhoon.org.cn (accessed on 6 March 2021). (**b**) Temporal evolution of Higos' intensity. The blue line indicates the central pressure from the best track data. The green line indicates the 2 min averaged maximum wind from the best track data. The vector arrows represent the VWS of 200–850 hPa, which is calculated by the wind shear within a 500 km radius of the typhoon center from the reanalysis data of the European Centre for Medium Range Weather Forecasts (ECMWF). The vertical orange rectangle represents the analyzing periods of this paper.

The traveled over offshore area in the South China Sea of Typhoon Higos was monitored by three radars located in the Pearl River Delta: Hong Kong Tate's Cairn Weather Radar, Zhuhai–Macao Weather Radar, and Shenzhen Weather Radar (Figure 1a). The time frequency of radar scanned-volume observation is 6 min. Table 1 displays the observation elevation angles and horizontal detection ranges of radial velocity of all radars. The Hong Kong Tate's Cairn Weather Radar has 10 layers of elevation observation in total, with the lowest detection elevation of 0.1°, the horizontal detection range of radial velocity below 5.4° being 256 km, and the horizontal detection range of upper elevation being 150 km. The Zhuhai–Macao Radar consists of 11 layers of elevation observation, with the lowest detection elevation of 0.1°, the horizontal detection range of radial velocity in the middle and lower elevation below 6.0° at 230 km, and the horizontal detection range of the upper elevation at 150 km. The Shenzhen Radar has 9 layers of elevation angles, with the lowest

detection elevation angle 0.5° and the horizontal detection range of the radial velocity at each elevation angle 150 km.

Table 1. Radial velocity observation elevation angles, ranges of three radars in the Pearl River Delta and other radar parameters.

Station (Code NO.)	Radial Velocity Elevation Angle and Detection Range	Wavelength/ Frequency	PRFs	Nyquist Velocity
Tate's Cairn, Hong Kong (45010)	0.1°0.9°1.8°2.7°3.6°5.4°(256 km) 9.9°15.0°22.0°34.0°(150 km)	2.845 G	585 Hz 999 Hz	45.0 m/s 51.6 m/s
Zhuhai-Macao (ZAR)	0.1°0.5°1.5°2.4°3.4°4.3°6.0°(230 km) 9.9°15.0°22.0°34.0°(150 km)	2.765 G	650 Hz 999 Hz	33.6 m/s 51.6 m/s
Shenzhen (Z9755)	0.5°1.5°2.4°3.3°4.3° (150 km) 6.0°9.9°14.6°19.5° (150 km)	2.765 G	1014 Hz 1282 Hz	27.7 m/s 32.3 m/s

Figure 2 shows the evolution characteristics of the three radars' reflectivity of Typhoon Higos at the height of 3 km in different periods from 17:00 to 20:00 UTC on 18 August 2020. The analyzing period is shown by a vertical orange rectangle in Figure 1b. During this period, the intensity change of Typhoon Higos is small, but the inner-core structure evolution is large. By analyzing the reflectivity at 17:00, 17:40, 18:00, 18:30 and 20:00 (Figure 2), one can see that the three-radar-observed reflectivity of the eyewall and rainband are the same in shape and basically the same in reflectivity intensity, but the Shenzhen radar gives a weak response, which may be caused by its calibration. We use the reflectivity of the Zhuhai–Macao Weather Radar as the input in the wind retrieval of the DDA method, so the weak response of Shenzhen's reflectivity does not affect the result of wind retrieval. The position of the typhoon center (red square box) is determined by the best-track typhoon center position. The VWS vector is shown by the red arrow. The speed of VWS is about 1 m/s, as shown in Figure 1b.

As illustrated in Figure 2a–c, the eyewall was small and unclosed at 17:00, and the broad echo located on the east-by-south side of the eyewall was vigorously active, which is the inner rainband. At the same time, another rainband developed weakly in the northeast and northwest sides, and the overall structure of the rainband was in a loose pattern, which is the outer rainband. The unclosed eyewall and inner rainband were located in the downshear zone of VWS, which is in line with the conclusions of the convective development of the downshear area of VWS [27–29]. Seen from Figure 2d–f, at 17:40, the inner rainband further developed to the downwind of the typhoon circulation, and at this time, the outer rainband developed significantly. The upwind convection of the outer rainband was more active, and the downwind stratiform portions are broadened. A remarkable phenomenon was a line of enhanced reflectivity developed in the stratiform sector of the outer rainband, as shown in the area marked by the bold red curve in the figure. Didlake et al. [19,20] found that the line of enhanced reflectivity and the broadening stratiform rainband were always a precursor to secondary eyewall development in a strong typhoon. Typhoon Higos did not experience the concentric eyewall formation, but the enhanced reflectivity line whirled inwardly, merged with the unclosed eyewall and spread outward.

In Figure 2g–i, at 18:00, the enhanced reflectivity line of the outer rainband began to merge with the unclosed eyewall. The red dot in the figure is their merging position. Then at 18:30 in Figure 2j–l, the merging had completed. By 20:00 in Figure 2m–o, the merged rainband whirled inwardly further, and the structure tightened up. The merged rainband was broadening obviously.

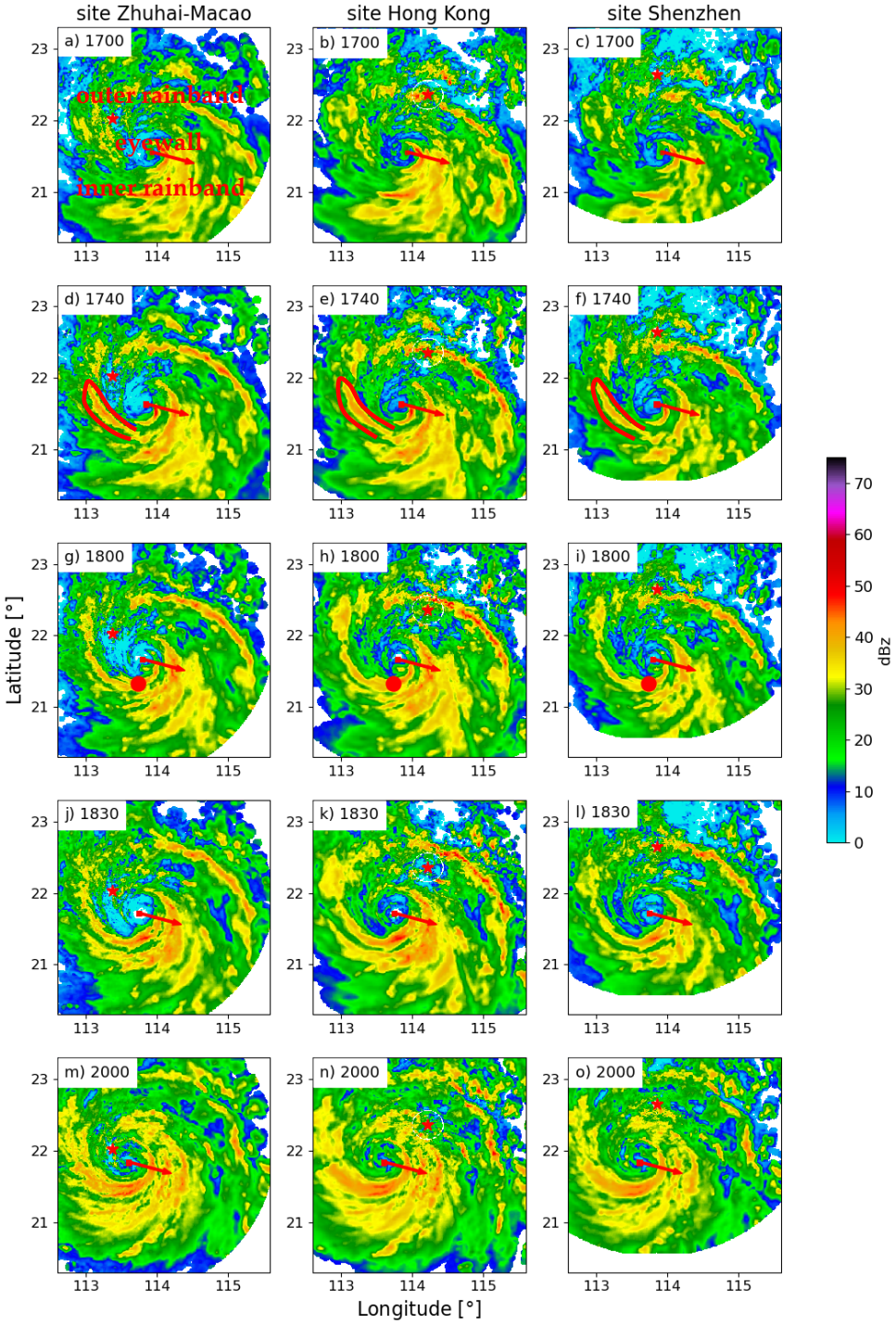

Figure 2. Reflectivity of Typhoon Higos at 3 km altitude observed by Zhuhai-Macau radar, Tate's Cairn radar in Hong Kong and Shenzhen radar at (**a**–**c**) 17:00, (**d**–**f**) 17:40, (**g**–**i**) 18:00, (**j**–**l**) 18:30 and (**m**–**o**) 20:00 UTC on 18 August 2020. The red stars represent the radar locations, the red square box represents the typhoon center and the red arrow is the VWS vector of 200–850 hPa. The three red characters in (**a**) indicate the approximate location of the eyewall, inner rainband and outer rainband.

3. Methods

3.1. The 3-D Variational Wind Field Retrieval Method

The three-dimensional (3-D) variational direct data assimilation Dual-Doppler analysis technique (DDA) given by Potvin [30] is adopted to calculate the wind field in the inner core of Typhoon Higos in this study. The inputs of the retrieval method include the reflectivity

factor (Z) and radial velocity (V_r) field in the Cartesian coordinate system, and the optimal wind field is obtained through the minimum cost function $J(u,v,w)$, thereby obtaining the vertical velocity. The $J(u,v,w)$ can be expressed as

$$J(u,v,w) = J_O + J_M + J_V + J_S \quad (1)$$

J_O is the observation equation term, which sums the root-mean-square (RMS) differences between the observed (v_{r1}^{obs} and v_{r2}^{obs}) and analyzed (v_{r1}^{a} *and* v_{r2}^{a}) radial wind from two radars, *Rad*1 *and Rad*2. It can be written as Equation (2).

$$J_O = \sum_{Rad1} \lambda_{O1} \left(v_{r1}^{obs} - v_{r1}^{a} \right)^2 + \sum_{Rad2} \lambda_{O2} \left(v_{r2}^{obs} - v_{r2}^{a} \right)^2 \quad (2)$$

J_M is the mass continuity equation term, written as Equation (3). ρ is the base-state atmospheric density, and the "Cart" label indicates that the summation is performed over the Cartesian analysis grid point.

$$J_M = \sum_{Cart} \lambda_M \left[\frac{\partial u^a}{\partial x} + \frac{\partial v^a}{\partial y} + \frac{\partial w^a}{\partial z} + \frac{w^a}{\rho} \frac{\partial \rho}{\partial z} \right]^2 \quad (3)$$

J_V is the vorticity equation term, written as Equation (4). ζ is vertical vorticity.

$$J_V = \sum_{cart} \lambda_v \left[\frac{D\zeta}{Dt} + (u^a - U) \frac{\partial \zeta^a}{\partial x} + (v^a - V) \frac{\partial \zeta^a}{\partial y} + (w^a) \frac{\partial \zeta^a}{\partial z} + \left(\frac{\partial v^a}{\partial z} \frac{\partial w^a}{\partial x} - \frac{\partial u^a}{\partial z} \frac{\partial w^a}{\partial y} \right) + \zeta^a \left(\frac{\partial u^a}{\partial x} + \frac{\partial v^a}{\partial y} \right) \right]^2 \quad (4)$$

J_S is the smoothing term, written as Equation (5).

$$\begin{aligned} J_S = {} & \sum_{cart} \lambda_{s1} \left[\left(\frac{\partial^2 u^a}{\partial x^2} \right)^2 + \left(\frac{\partial^2 u^a}{\partial y^2} \right)^2 + \left(\frac{\partial^2 v^a}{\partial x^2} \right)^2 + \left(\frac{\partial^2 v^a}{\partial y^2} \right)^2 \right] + \sum_{cart} \lambda_{s2} \left[\left(\frac{\partial^2 u^a}{\partial z^2} \right)^2 + \left(\frac{\partial^2 v^a}{\partial z^2} \right)^2 \right] \\ & + \sum_{cart} \lambda_{s3} \left[\left(\frac{\partial^2 w^a}{\partial x^2} \right)^2 + \left(\frac{\partial^2 w^a}{\partial y^2} \right)^2 \right] + \sum_{cart} \lambda_{s4} \left[\left(\frac{\partial^2 w^a}{\partial z^2} \right)^2 \right] \end{aligned} \quad (5)$$

The constraint minimizes second-order spatial derivatives in u^a, v^a, w^a and, therefore, serves both to dampen small-scale noise and to extend analyzed wind gradients into data-spare regions, where λ is the weight of each cost function, λ_O, λ_M, λ_v, λ_s equal to 1.0, 1500, 1.0, and 1.0 separately in this paper. The reflectivity factor (Z) is used to estimate the fall speed of the precipitation particle by the methodology of Mike Biggerstaff and Dan Betten in the Potvin [30] paper and then to compute the vertical velocity of air.

The research findings indicated that the DDA method has a high accuracy of horizontal wind retrieval, but the retrieval accuracy of vertical velocity is greatly affected by factors such as the elevation angle layer and the sampling time of the radar volume coverage pattern (VCP) [31,32]. In this paper, the wind field in the inner-core area of Typhoon Higos is retrieved by the DDA method, based on the high-density radar network in the Pearl River Delta. The VCP sampling time is designed to be about 6 min, but the Plan Position Indicator (PPI) observations at the lowest elevation (0.1°) and the highest elevation (34°) of Hong Kong Tate's Cairn radar and the Zhuhai–Macao radar are both higher than those of the traditional radar VCP21 model at the minimum elevation (0.5°) and the maximum elevation (19.5°) (Table 1), which is beneficial to improving the accuracy of wind retrieval. At the same time, the observation radius of the horizontal radial velocity of the two radars at a low elevation angle is 230 km, which also creates somewhat better conditions for acquiring the wind field in the inner-core area of the typhoon from a long distance. Therefore, before retrieving the wind field of Typhoon Higos using the three radars' observation, we carry out an OSSE to validate the retrieval accuracy of the vertical velocity by the DDA method, as shown in Section 3.2.

3.2. Validation of DDA Method for Retrieving Vertical Velocity

Figure 3 is the OSSE flow chart. First, the WRF model simulates Typhoon Higos. Then, the wind u, v, w and cloud precipitation microphysics data of WRF-out will input into the radar emulation software CR-SIM made by the State University of New York at Stony Brook [33]. After setting the radar band, beam width, observation mode and other radar parameters for CR-SIM, the radar radial velocity and reflectivity will be emulated out and then used to calculate the emulated wind field by the DDA method. Last, the emulated vertical velocity will be compared with the WRF-out w (as truth) in order to verify the accuracy of the DDA method in retrieving the vertical velocity of Typhoon Higos.

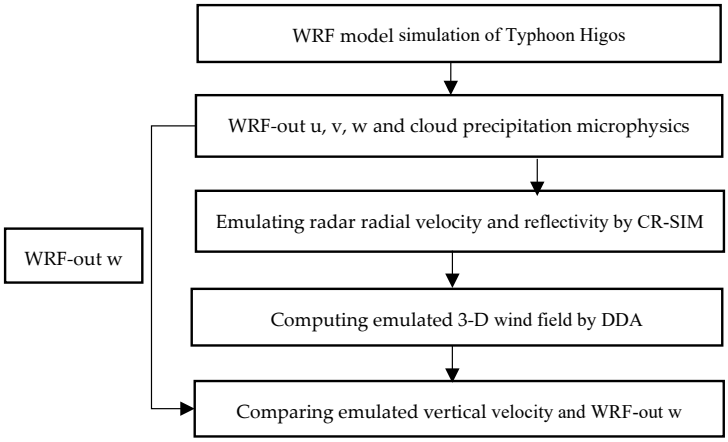

Figure 3. A flow chart of OSSE for validating the retrieval accuracy of the vertical velocity by the DDA method.

Two interactive, nested domains (12/3 km) are adopted for the simulation of Typhoon Higos by the WRF model, and the driving data are the ECMWF Reanalysis v5 (ERA5) 0.25° × 0.25° reanalysis data, and the simulation period of time is from 12:00 to 24:00 UTC on 18 August 2020. The model top is set at 10 hPa, and 51 sigma layers are used in the vertical direction. The single-moment, 6-class (WSM6) microphysics parameterization scheme [34] performs better than other schemes in simulating a rapid intensification (RI) typhoon [35–37]. The model configuration with regards to other physical processes is given in Table 2. The simulated track and intensity are compared with the best track and intensity of Typhoon Higos in Figure 4. The distance between the Tate's Cairn Radar in Hong Kong and the Zhuhai–Macao Radar is 94.7 km. It can be seen from the figure that the center position of the simulated typhoon is about 1–2 h behind that of the actual typhoon in time, and the intensity of the simulated typhoon fails to reach the scale of the typhoon, i.e., it is weaker than the actual typhoon. This has little influence on verifying the reliability of the DDA method to retrieve the vertical velocity of Typhoon Higos, because the WRF-simulated typhoon center position and the actual optimal path position in the period from 17:00 to 20:00 analyzed in this paper are within the optimal range of dual radars retrieval [38].

Figure 5 displays the emulated reflectivity and radial velocity of Tate's Cairn weather radar at 0.9° elevation at 18:00 UTC on the 18th. Compared with the actual observation at 18:00 on the 18th of Tate's Cairn radar in Figure 2h, the emulated radar reflectivity is looser than the actual observed structure, and the typhoon eye is also not clear enough, but the convection of the eyewall and the rainband are obvious, which can be used to test and analyze the reliability of the DDA to retrieve the vertical velocity.

Table 2. Model configuration for the control experiment.

Domain	D01	D02
Horizontal grid number	180 × 153	520 × 356
Grid spacing (km)	12	3
Integration time (h)	12	12
Cumulus parameterization	Kain-Fritsch Scheme	
Microphysics	Single-moment 6-class	
Planetary boundary layer	Yonsei University scheme	
Radiation Scheme	Rapid and Accurate Radiative Transfer Model	

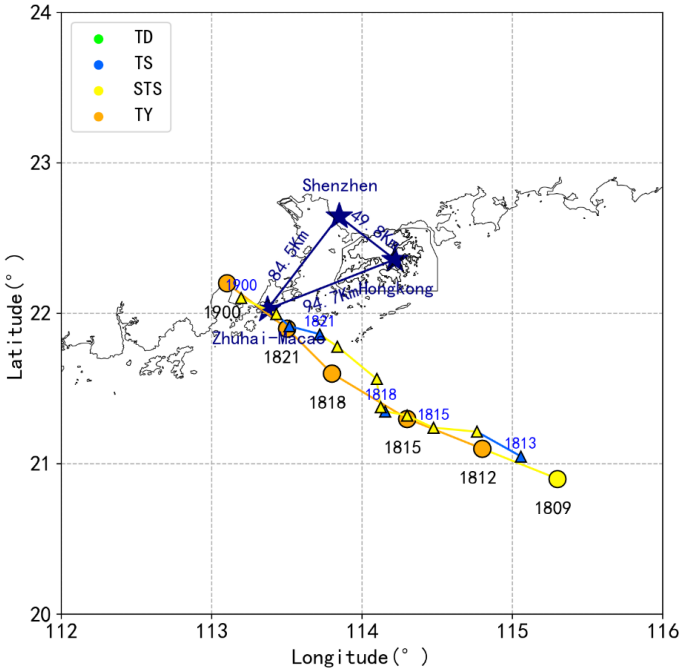

Figure 4. Comparison of simulated track (line with triangles) and intensity (colored) with best track (line with circled dots) and intensity (colored) of Typhoon Higos.

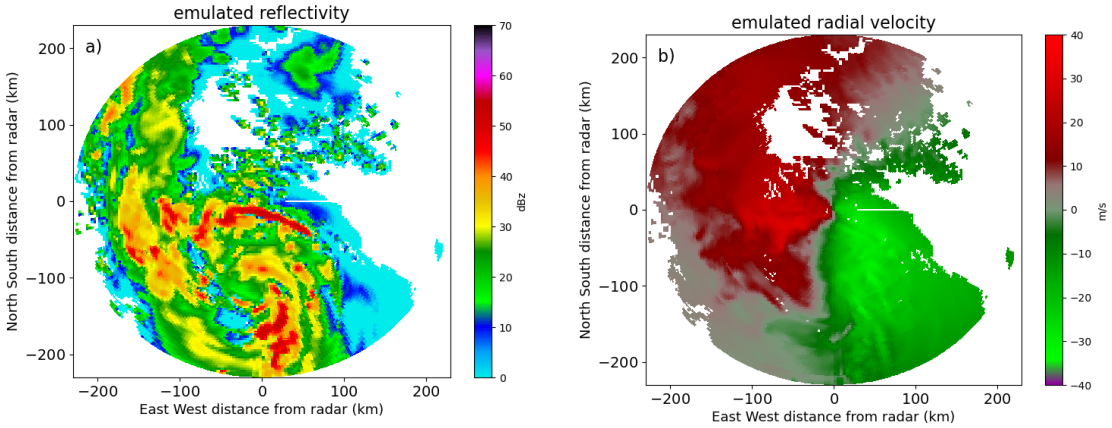

Figure 5. The emulated (**a**) reflectivity and (**b**) radial velocity of Hong Kong Tate's Cairn weather radar at 0.9° elevation at 18:00 UTC 18 August 2020. Coordinate point [0, 0] is the location of the radar.

Based on the CR-SIM software emulation of HK Tate's Cairn radar and Zhuhai radar at 17:00, 18:00 and 19:00, we retrieve the emulated three-dimensional wind field of Typhoon Higos by using the DDA method. Figure 6 shows the comparison between the emulated vertical velocity w at 5 km altitude retrieved by the DDA and the vertical velocity w of WRF-out at 5 km altitude at the 3 moments. Figure 7 is the statistical scatters of the correlation between the two vertical velocity w's of Figure 6, point to point. We can see that the overall

trends of the emulated speed values retrieved by the DDA method in Figure 6a,c,e are basically similar to those of WRF-out in Figure 6b,d,f, especially the WRF-out w rising speed (warm color) value larger than 2 m/s. However, when the WRF-out w value is small, the emulated w by the DDA is slightly larger than WRF-out, whether rising speed or sinking speed, which corresponds to the majority scatters gathering among −1.5 m/s and 1.5 m/s of WRF-out w, presenting a horizontal rugby shape in Figure 7a. The correlation coefficient (CC) of the total point is only 0.51 in Figure 7a, and the CC is also relatively low at 0.50 when filtering the points, which are the emulated w values below 2 m/s or the WRF-out w values below 2 m/s in Figure 7b. Yet, the t values of the *t*-test are good, −1.36 and −1.91, separately in Figure 7a,b. Vertical velocity is a physical quantity that is always difficult to measure or retrieve. The OSSE results show that the vertical velocity retrieved by the DDA method is comparable with the reference value (WRF-out w). Although there are still some differences in the value, they do not affect the qualitative understanding of Typhoon Higos' active dynamic evolution, and the vertical velocity characteristic is quite necessary to be recognized.

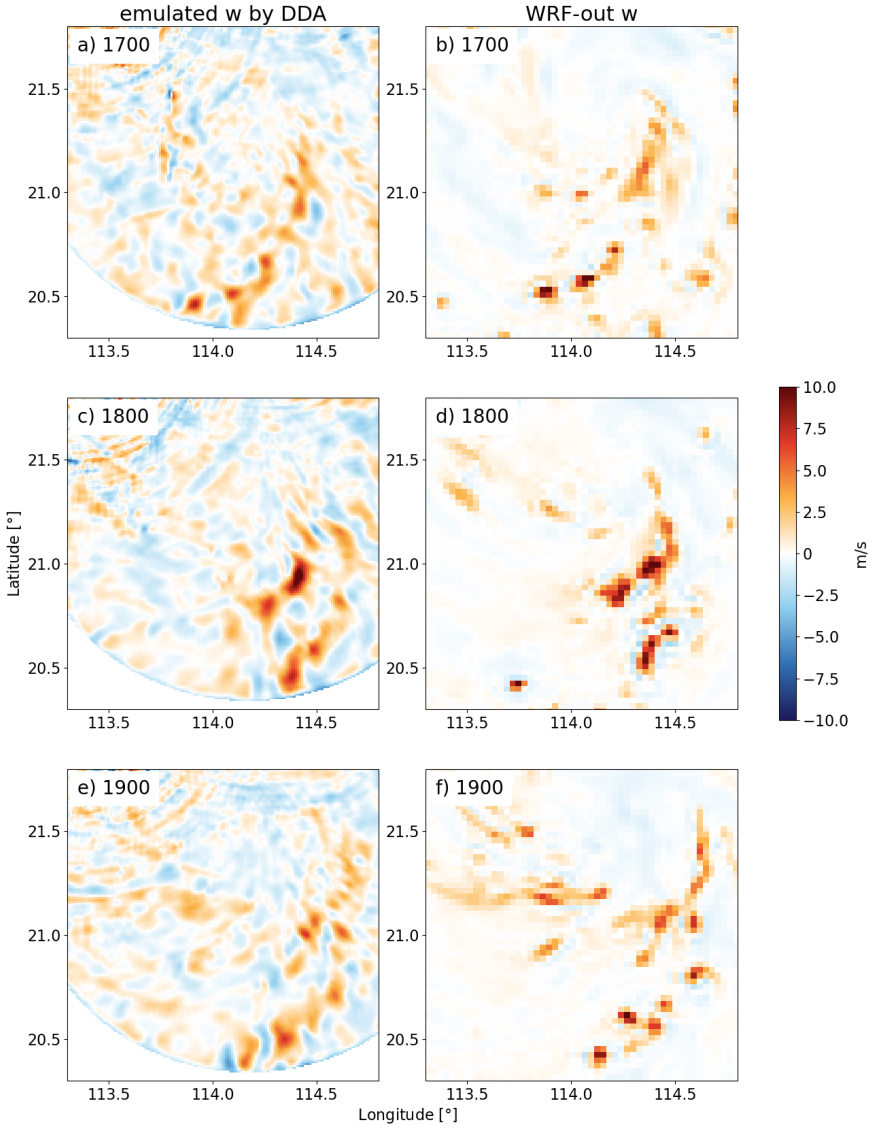

Figure 6. Comparison of the vertical velocity at 5 km altitude (**a**,**c**,**e**) of Typhoon Higos retrieved by the DDA method based on the CR-SIM-emulated radial velocities from Zhuhai–Macao radar and HK Tate's Cairn radar with the vertical velocity w at 5 km altitude (**b**,**d**,**f**) from WRF-out at (**a**,**b**) 17:00, (**c**,**d**) 18:00 and (**e**,**f**) 19:00 UTC. The warm color is rising speed. The cold color is sinking speed.

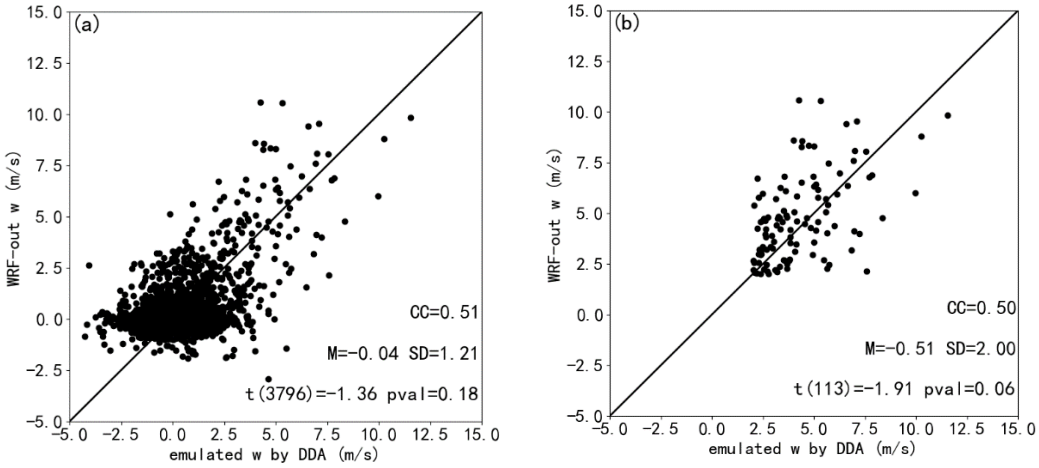

Figure 7. The point-to-point statistical scatters of correlation between the emulated w by the DDA method and WRF-out w. (**a**) The analysis time is the same as Figure 6, 17:00, 18:00 and 19:00. (**b**) The same as (**a**), except for filtering the points that are emulated w values below 2 m/s or WRF-out w values below 2 m/s. CC is the correlation coefficient of two w. M is the mean of difference. SD is the standard deviation. The t and pval are the t-test results.

4. Results and Discussion

After the reliability validation of the DDA method in Section 3.2, we use the actual observations of Zhuhai–Macao radar, HK Tate's Cairn radar and Shenzhen radar to retrieve the three-dimensional (3-D) wind fields of Typhoon Higos at the four moments given in Figure 2 by the DDA method for analyzing dynamic features. The Zhuhai–Macao radar and HK Tate's Cairn radar are responsible for the retrieval of the wind fields of Typhoon Higos at 17:00, 18:00 and 19:00. The typhoon center approaches the Zhuhai–Macao radar by 20:00, and the retrieval of the wind field in the typhoon core area is significantly affected by the cone of silence of the Zhuhai–Macao radar. At this time, Shenzhen radar is employed to make up for the observation in the cone of silence. Thus, the three radars, namely, HK Tate's Cairn radar, Zhuhai–Macao radar and Shenzhen radar, have jointly retrieved the wind field at 20:00 on the 18th.

4.1. Analysis of Horizontal Wind

Figure 8 shows the horizontal wind at the height of 4 km in the inner-core area of Typhoon Higos. As seen in Figure 8a–d, the strong and broad reflectivity developed in the southeast quadrant corresponds to the wide range of the southwest wind. Analyzing the synoptic chart (not displayed in paper), the obvious southwest wind is affected by southwest monsoon flow. The large-value wind speed in the typhoon inner-core area develops at 17:00 from the right area of the VWS vector to the left area, and it reaches the maximum on the left side in Figure 8a. Then, it gradually shows down as the circulation develops downwind. This retrieval result is consistent with the conclusion of Reasor and Rogers [28] on the influence of VWS on typhoon structure, and also qualitatively verifies the reliability of the horizontal wind of Typhoon Higos. The red, bold, U-shaped curves in Figure 8b–d are used to mark the end of the stratiform rainband with wind speed greater than 20 m/s. In Figure 8b, the wind speed at the end of the stratiform rainband increases first, and the enhanced reflectivity line begins to merge with the unclosed eyewall. Figure 8c shows that the large-value wind speed at the end of the stratiform rainband is developing to an upwind direction. At 20:00, after the enhanced reflectivity line is completely merged with the eyewall, the wind speed and echo intensity both increase significantly (Figure 8d). The wind speed at the end of the stratiform sector of the outer rainband in Typhoon Higos increases first and then develops to the upwind direction.

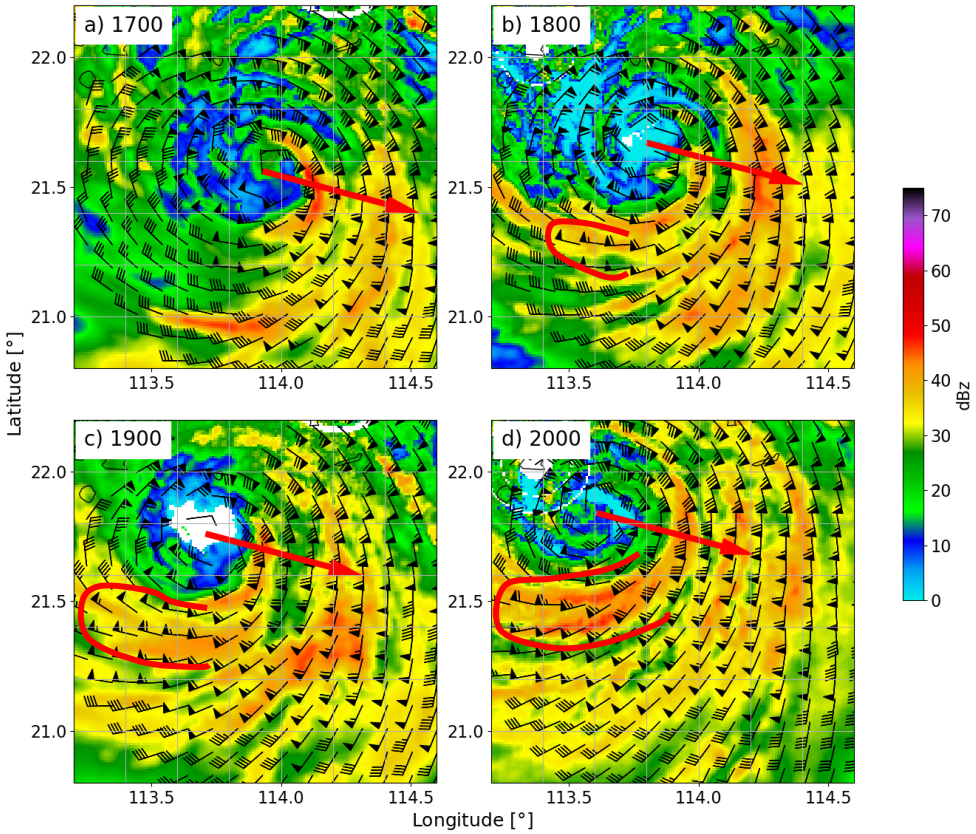

Figure 8. The horizontal winds at 4 km altitude in the inner-core area of Typhoon Higos retrieved by Zhuhai–Macao radar, HK Tate's Cairn radar and Shenzhen radar at (**a**) 17:00, (**b**) 18:00, (**c**) 19:00 and (**d**) 20:00 UTC on 18 August 2020. In the figure, the 4 km altitude reflectivity at the four moments are superimposed. Red arrows represent the VWS vector of 200–850 hPa. The black triangles in the wind barbs represent the wind speed at 20 m/s, the long rods represent 4 m/s and the short rods 2 m/s.

Didlake et al. [19] concluded that the convergence generated by mesoscale sinking inflow in the radial direction of the middle troposphere of the stratiform rainband would increase the velocity of the enhanced reflectivity line. Now, taking the center of Typhoon Higos as the central point, we calculate the radial velocity component of the typhoon horizontal circulation and analyze the inflow and outflow of the radial velocity in the core area of the typhoon. The position of the typhoon center is determined by that of the best-track typhoon center. Figure 9 shows the radial wind calculated from the horizontal wind in Figure 8, with warm colors as inflow and cool colors as outflow. It can be seen from Figure 9a–d that at the 4 km altitude in the typhoon inner-core area, there are obvious inflows in the southeast quadrant of the typhoon center, outflows in the northeast quadrant, inflows in the northwest quadrant, and outflows in the southwest quadrant. These radial inflows and outflows alternate with the change of the azimuth. The radial inflow in the southeast quadrant is related to the southwest monsoon, which indicates the influence of the monsoon develops to the southwest side with time. The radial outflow and inflow in the southwest quadrant in Figure 9c,d converge at the latitude of about 21.4°, which corresponds to the enhanced reflectivity line position in Figure 8. To further analyze the dynamic radial wind inflow and outflow of the stratiform rainband, the rainband is divided into the upwind of the stratiform rainband with an azimuth of 270–340° and the downwind of the stratiform rainband with an azimuth at 190–240°, as shown by the dashed line in Figure 9a. The azimuths' selection comprehensively considers the reflectivity evolution positions of the upwind and downwind from 17:00 to 20:00 in Figure 2. At the same time, to avoid mutual influence during calculation, the azimuth of the upwind and downwind are separated by 30°. The upwind of the stratiform rainband corresponds to the stratiform

rainband with a very wide horizontal range, and the downwind of the stratiform rainband corresponds to the position of the enhanced reflectivity line. The radial winds and vertical velocity corresponding to the upwind and downwind are respectively averaged by azimuth in the following text to analyze the variance of the dynamic characteristics with the radius range varying. The tangential winds are averaged by the radius range to analyze the variance of the dynamic characteristics azimuthally. The radius range means the horizontal range to the typhoon center.

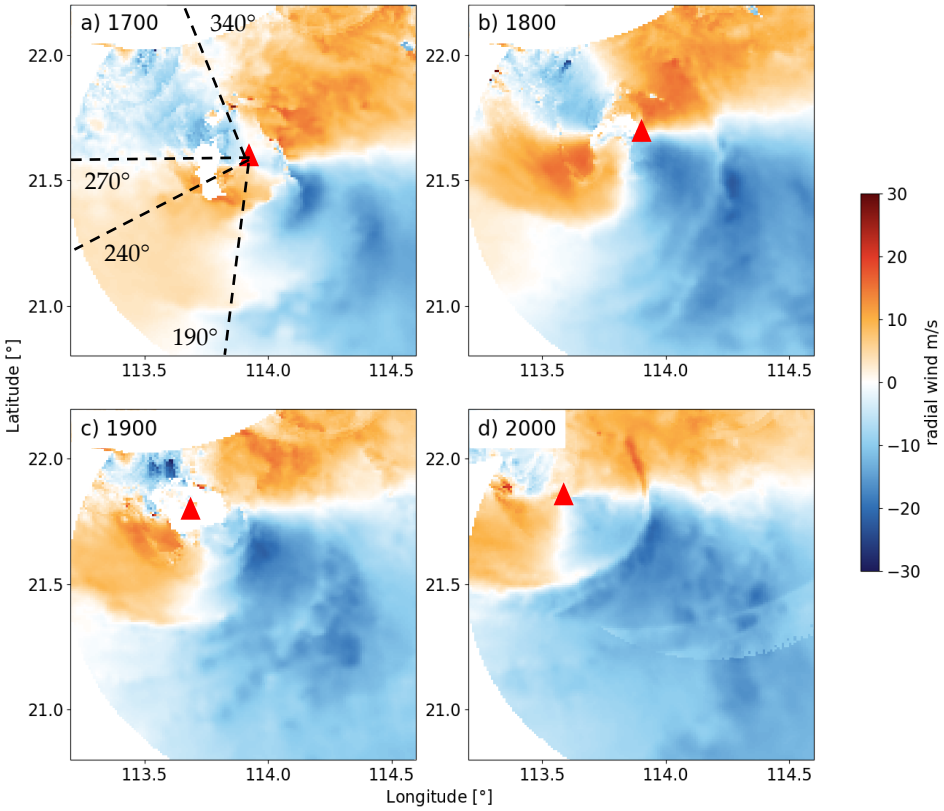

Figure 9. Radial wind calculated based on the horizontal wind at 4 km altitude in Figure 8 with the typhoon center as polar coordinate center point at (**a**) 17:00, (**b**) 18:00, (**c**) 19:00 and (**d**) 20:00 UTC on 18 August 2020. The red triangle represents the typhoon center; the cool color and warm color represent the inflow and outflow of the radial wind, respectively; and the dashed line marks the azimuth positions of the upwind and downwind of stratiform rainband in the outer rainband of Typhoon Higos.

Figure 10 shows the changes of the average radial wind at 270–340° in the upwind of the stratiform rainband with the outward horizontal radius and height of Typhoon Higos' center at above four times. The eyewall and rainband can be distinguished by the reflectivity isoline. In Figure 10a, the maximum inflow in the lower layer is located in the horizontal radius range of 10–20 km, which is the position of the eyewall, while in the range 30–60 km of the radius is the upwind of the stratiform rainband. There is weak inflow at the 2.5–5 km altitude of the upwind of the stratiform rainband and also in the boundary layer. Then, in Figure 10b, we can see in the radius range of 50–60 km and at the height of about 7.5 km, there is sinking inflow, and meanwhile, the rising outflow at the inner side of the same height is enhanced, forming an obvious secondary circulation. The secondary circulation of this rainband makes the height of the isoline obviously higher than that of the radius of 30–40 km. At the radius of 50–60 km, the inflow is also enhanced at the height of about 1 km. In Figure 10c, an obvious inflow flows in the lower troposphere within the height of about 3 km and the radius of 40–60 km, and an outflow develops in the upper level of the inflow, but an inflow develops in the middle troposphere at the height of 5 km.

Within the radius of 30–60 km in Figure 9d, there is an obvious sinking development of the mid-layer inflow and rising outflow in the top layer, and the characteristics of the inflow at 1 km height and the outflow at 2.5 km height are also more significant. This phenomenon of Typhoon Higos is consistent with the dynamic characteristics of the stratiform rainband proposed by Qiu and Tan [4] and Didlake et al. [19,20].

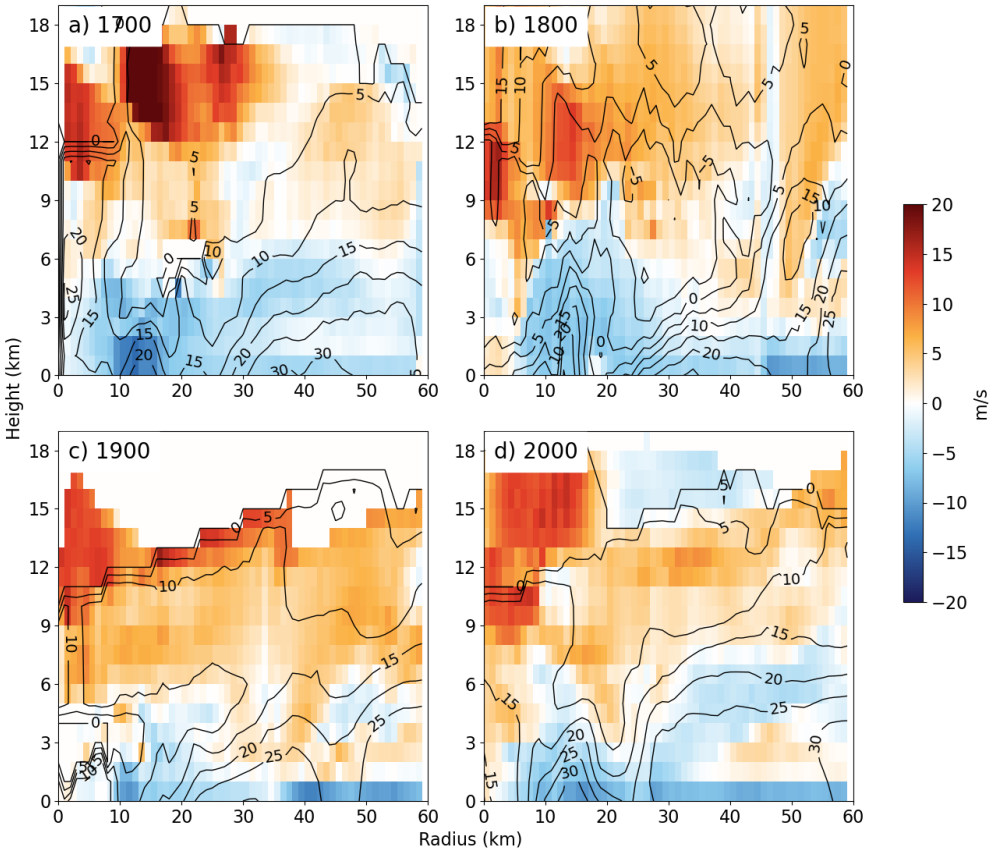

Figure 10. Variations of the radial wind (color shading) and reflectivity (black contour) azimuth means in the upwind of stratiform rainband at 270–340° with horizontal radius of 0–60 km outward from typhoon center with altitude at (**a**) 17:00, (**b**) 18:00, (**c**) 19:00 and (**d**) 20:00 UTC. The cool color of radial wind azimuth mean represents the inflow and the warm color the outflow.

Figure 11 shows the variation of the average radial wind at the downwind azimuth of 190–240° with the outward horizontal radius and height of Typhoon Higos' center. There are obvious differences at the corresponding time between Figures 11a–d and 10a–d. The average azimuth radial wind at the downwind of stratiform rainband is dominated by outflow, and the outflow speed at the upper layer increases considerably. The characteristics radial wind in the middle and lower troposphere in the downwind of the stratiform rainband are also clearly distinct from those in the upwind. There is no sinking inflow in the middle layer of the downwind of the stratiform rainband. At 19:00 and 20:00, inflow appears in the middle and lower troposphere with a radius of 40–60 km, but it is obviously different from the lower troposphere inflow in the upwind of the stratiform rainband and an outflow aloft the inflow. Figure 11b–d denote that the outflow speed at the radius of 10–30 km with height below 5 km is greater than 10 m/s, and the large outflow velocity is located inside the stratiform rainband, where the reflectivity isolines are dense and the isolines rise up steeply outward with the radius, which is the cause for the enhanced reflectivity line. At 19:00 and 20:00, the inflow in the middle and lower troposphere with a radius of 40–60 km is related to the westward development of the radial inflow with the southwest monsoon developed in Figure 9c,d, and it converges with the outflow from the

radius range of 10–30 km, which is the reason for the enhanced reflectivity line developed and the speed value increases at the end of the line first.

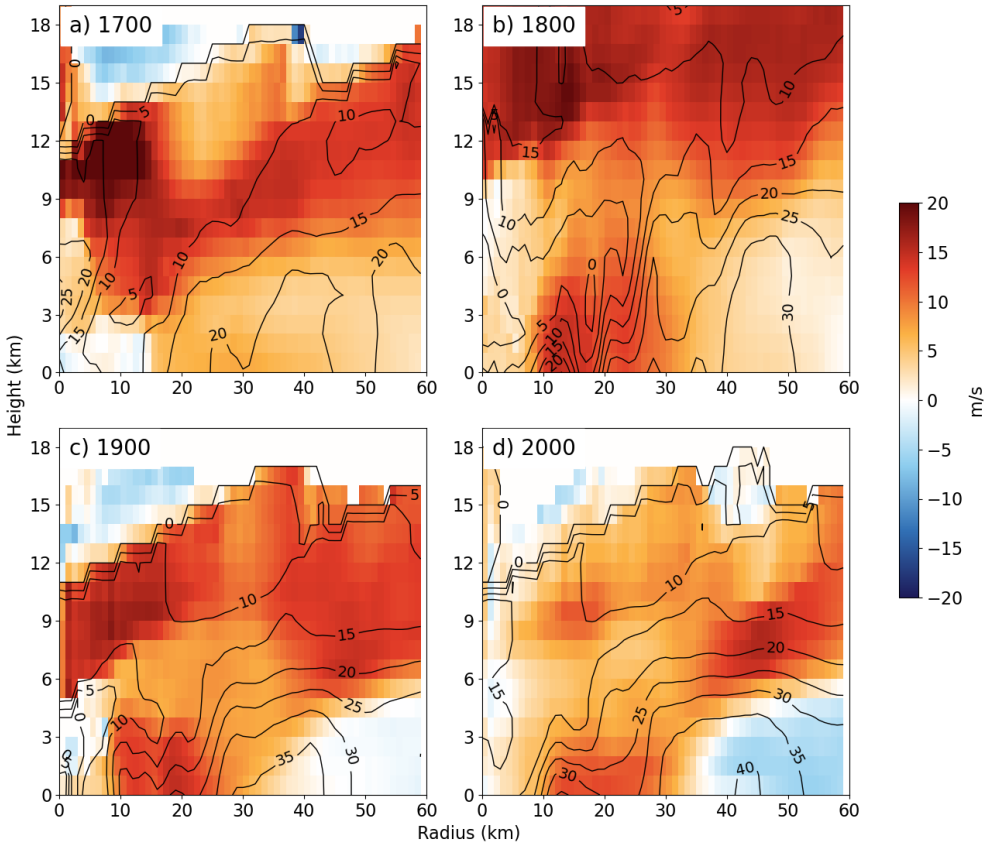

Figure 11. Variations of the radial wind (color shading) and reflectivity (black contour) azimuth means in the downwind of stratiform rainband at 190–240° with horizontal radius of 0–60 km outward from typhoon center with altitude at (**a**) 17:00, (**b**) 18:00, (**c**) 19:00 and (**d**) 20:00 UTC. The negative value of radial wind azimuth mean represents the inflow and the positive value the outflow.

Figure 12 shows the change of the range average of the tangential wind of 20–60 km radius outward from Typhoon Higos' center with the height of the stratiform rainband at the azimuth of 190–340° at four moments. At the azimuth 270–340° in the upwind of the stratiform rainband, in Figure 12b, the range of the tangential wind beyond 20 m/s in the middle and lower troposphere is remarkably increased and the tangential wind in the upper troposphere is also increased compared with those in Figure 12a, which is related to the enhancement of inflows in the middle and lower troposphere in Figure 9b. In addition, with the further enhancement of the mid-layer inflow, the tangential wind value of the lower layer at the azimuth 270–340° in Figure 11c,d also increases further. At 19:00, the tangential wind in the lower troposphere becomes stronger than 25 m/s, and by 20:00, the maximum wind speed reaches more than 30 m/s, but the high wind speed develops towards the downwind of the circulation. In the upwind of the stratiform rainband, the sinking inflow in the middle troposphere strengthens, and the tangential wind in the lower troposphere is enhanced, spreading to the downwind, which is consistent with the research results of Didlake and Houze [19,20]. However, as shown in Figure 12b–d, the tangential wind at the azimuth 210–240° is not increasing, and it means that the large tangential wind speed in the upwind of the stratiform rainband has not been completely transferred into the downwind area.

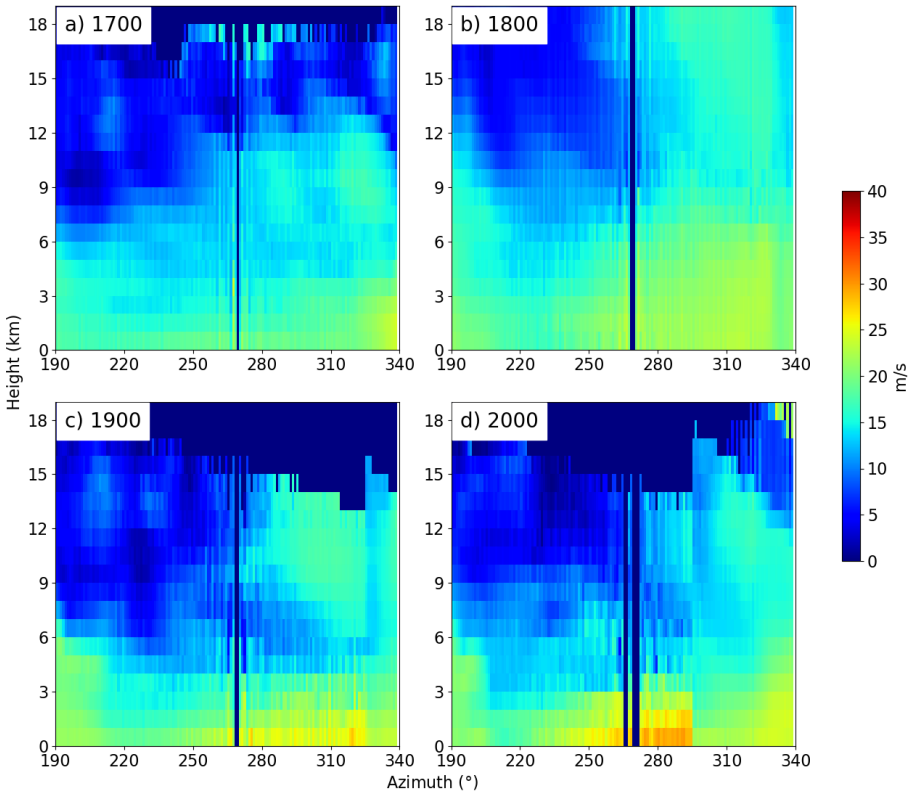

Figure 12. Variation of the tangential wind range mean (color shading) of the stratiform sector of outer rainband at azimuth 190–340° with horizontal radius of 20–60 km outward from the Typhoon Higos center with altitude at (**a**) 17:00, (**b**) 18:00, (**c**) 19:00 and (**d**) 20:00 UTC. The vacancy at azimuth around 270° indicates that averaged tangential wind cannot be obtained.

4.2. Analysis of Vertical Velocity

Qiu and Tan [4] and Didlake et al. [19,20] believe that the sinking inflow in the middle troposphere of the stratiform rainband is mainly caused by latent heat cooling, such as melting of ice particles and evaporation of liquid water. Figure 13 shows the changes of the vertical velocity azimuth average in the upwind of the stratiform rainband, with Typhoon Higos' center radius being 60 km with altitude. In Figure 13a, the rainband area with a radius of 30–60 km is dominated by updraft, while the middle and upper troposphere with a radius of 10–30 km is dominated by downdraft. From the reflectivity isolines, we can see that the updraft of the rainband area corresponds to the enhanced reflectivity, but the reflectivity of the downdraft is small. The typhoon eye area with a radius less than 10 km has significant updraft in the outer side, while the airflows in the inner side are rising in the middle and lower troposphere, but sinking in the upper troposphere. In Figure 13b, the middle layer with a radius of 50–60 km, which corresponds to the downdraft of the middle troposphere of the upwind of stratiform rainband in Figure 10b, has an inclined downdraft and an updraft adjacent to its inner side. In the typhoon eye area, the downdraft is dominant in the middle and lower troposphere, and the updraft in the upper troposphere. As shown in Figure 13c, in the same position of sinking inflow in the middle troposphere of the upwind of the stratiform rainband in Figure 9c, there is an inclined downdraft in the outer side of the radius of 40–60 km and a significant updraft in the inner side. The typhoon eye is dominated by downdraft, and there is also an obvious clear sky in the eye of the typhoon, as shown in Figure 8c. In Figure 13d, there is downdraft at the height of 2.5–6 km and the radius of 30–40 km, which is also corresponding to the downdraft position of the midlevel inflow in the upwind of the stratiform rainband in Figure 10d, and there is clearly noticeable updraft in the middle and upper troposphere of the inner side of the 20–30 km radius. In addition, it can be seen from Figure 12 that the sinking inflows in the middle

troposphere of the stratiform rainband all have downdraft corresponding to them, and there is corresponding development of updraft near the inner side of the downdraft.

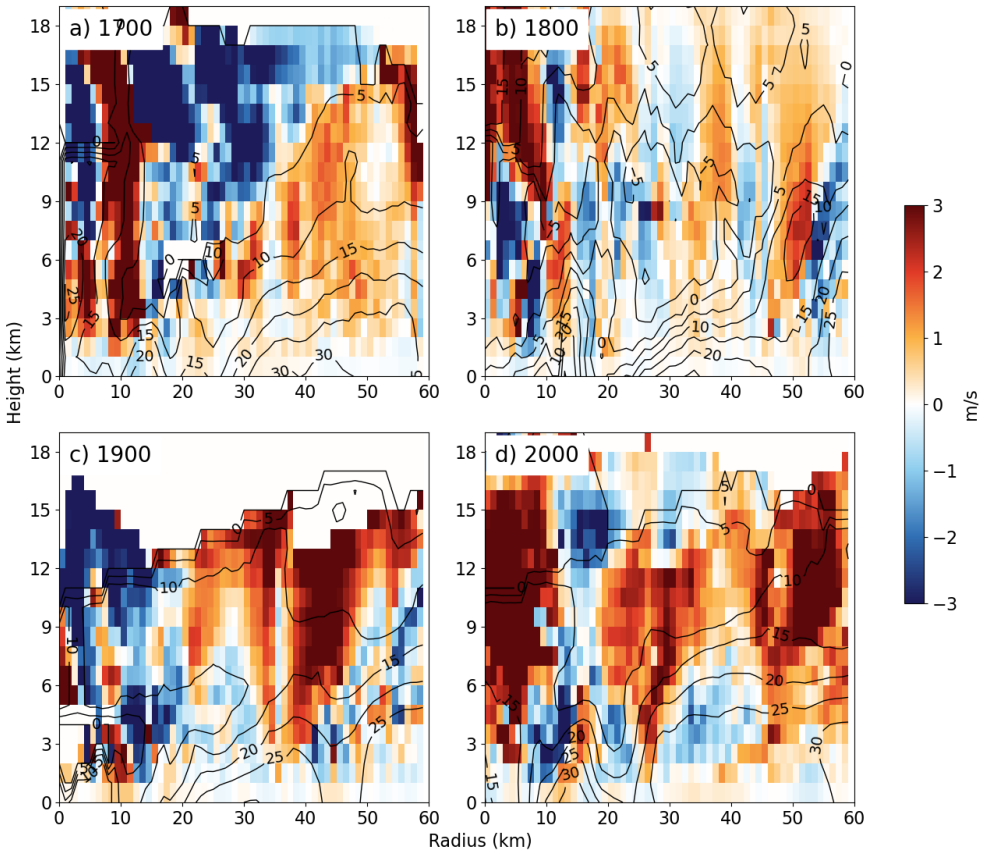

Figure 13. Variations of the vertical velocity (color shading) and reflectivity (black contour) azimuth means in the upwind of stratiform rainband at 270–340° with horizontal radius of 0–60 km outward from typhoon center with altitude at (**a**) 17:00, (**b**) 18:00, (**c**) 19:00 and (**d**) 20:00 UTC. The negative value of vertical velocity azimuth mean represents the downdraft and the positive value the updraft.

Figure 14 presents the changes with altitude of the vertical velocity azimuth average in the downwind of the stratiform rainband, with the center radius being 60 km of Typhoon Higos. Figure 14a is similar to Figure 13a in the vertical velocity characteristics of the upwind of the stratiform rainband, that is, updraft mainly within the radius range of 20–60 km, with weaker downdraft in the upper layer. Figure 14b reveals that the vertical velocity is represented by downdraft within the radius range of 50–60 km at each altitude layer, but updraft within the radius of 30–50 km. Its characteristics significantly differ from that of Figure 13b, and the downdraft is not inclined. In Figure 14c,d, there are no inclined descending airflows in the middle troposphere layer of the downwind of the stratiform rainband within the radius of 20–60 km, but it is dominated by updraft, with significant vertical velocity developing upward at the altitude of about 5 km within the radius range of 30–40 km. This position matches with the convergence of the strong low-level outflow from inside the rainband and the monsoon-related southwesterly inflow in the outer side in Figure 11c,d, and the downwind reflectivity of the stratiform rainband is also obviously enhanced in this area. It is the downdraft in the middle and lower troposphere within radius of 10–20 km that leads to the strong outflow in the lower troposphere. The vertical velocity analysis further indicates that the dynamic developing mechanisms of the upwind and downwind sections of the stratiform rainband are evidently distinct. The development of the stratiform rainband is caused by the convergence of outflow from inside the rainband and the inflow from outside wind related to the southwest monsoon developing westward with time.

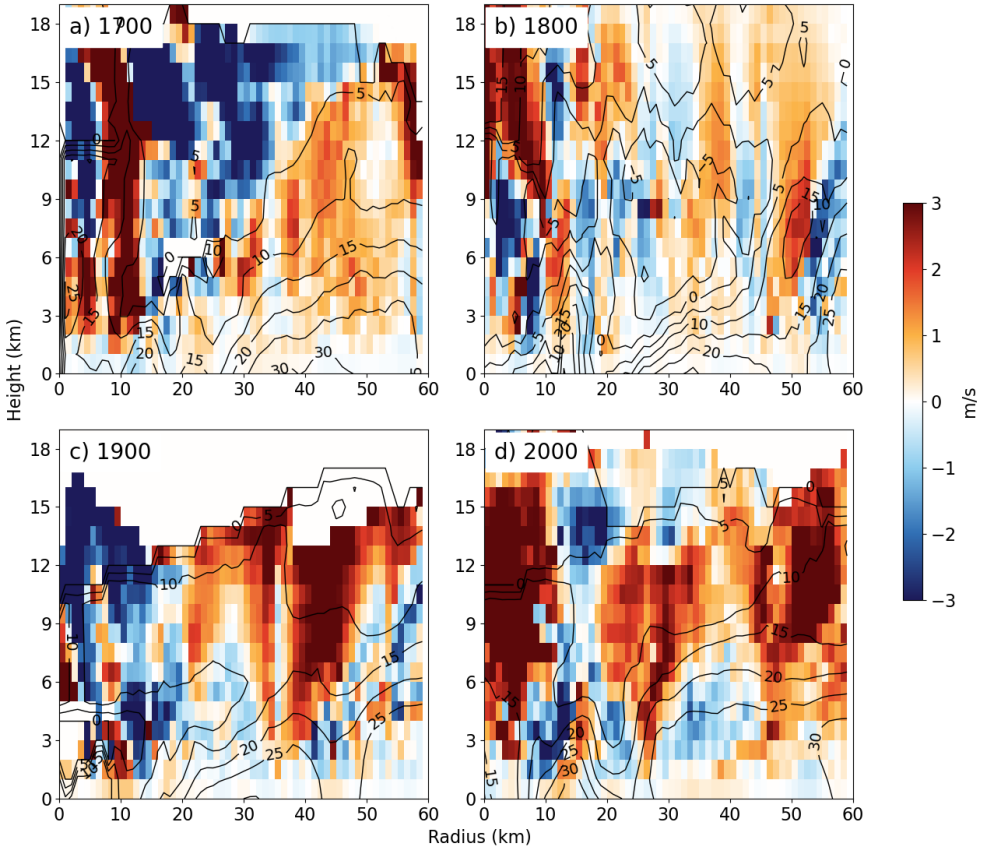

Figure 14. Variations of the vertical velocity (color shading) and reflectivity (black contour) azimuth means in the downwind of stratiform rainband at 190–240° with horizontal radius of 0–60 km outward from typhoon center with altitude at (**a**) 17:00, (**b**) 18:00, (**c**) 19:00 and (**d**) 20:00 UTC. The negative value of vertical velocity azimuth mean represents the downdraft and the positive value the updraft.

5. Conclusions

Based on the observation of densely distributed ground-based weather radars in the Pearl River Delta, this paper has retrieved the dynamic field of the inner core of Typhoon Higos in the offshore area by using the DDA wind field retrieval method. Prior to the retrieval, the OSSE was carried out to validate the reliability of retrieved data by the DDA method. Then, our paper has also analyzed the dynamic characteristics of the upwind and downwind of the stratiform rainband when the rainband whirled inwardly, merged with the unclosed eyewall and spread outward, but its structure was asymmetric between the upwind and downwind, which makes us further understand the mechanism of the structure evolution in the typhoon's inner core. Our analysis is summarized in the conceptual model shown in Figure 15. The main conclusions are as follows:

(1) The Hong Kong Tate's Cairn radar, Zhuhai–Macao radar and Shenzhen radar can successfully observe the evolution of the offshore structure of Typhoon Higos. Through the DDA wind field retrieved, the refined dynamic field structures of the inner-core area of Typhoon Higos offshore and its continuous evolution can be obtained. The OSSE, which is emulated radar based on WRF simulating Typhoon Higos out, shows that the emulated vertical velocity retrieved by the DDA is comparable.

(2) The dynamic structure of the stratiform sector of the outer rainband is significant during the offshore time of Typhoon Higos. Figure 15a shows that in the upwind of the stratiform area, the mesoscale sinking inflow in the middle troposphere and rising outflow in the top layer form the secondary circulation. There are the vortex-scale inflows in the lower troposphere, with an outflow aloft the inflow. These features are all in line with the

dynamic characteristics of the stratiform rainband in the forming process of the concentric eyewalls in strong typhoons concluded by previous scientists. However, the dynamic characteristics of the downwind of stratiform areas in Figure 15b are different from those in the upwind of stratiform areas, which is mainly affected by the vortex-scale inflow from outside the southwesterly wind and outflow from inside the rainband. The development of the southwesterly wind is promoted by the southwest monsoon. Tangential wind in the stratiform area of the outer rainband increases, as the plus signs show.

(3) The analysis of the vertical velocity characteristics of the upwind and downwind of the stratiform rainband suggests that there is an inclined downdraft at the position where the vertical velocity of the upwind of the stratiform rainband corresponds to the sinking inflow in the middle troposphere, indicated by the blue arrow in Figure 15a, and moreover, there is an accompanying updraft beside the downdraft indicated by the red arrow. The vertical velocity of the downwind of the stratiform rainband in Figure 15b is featured with updraft, which is different from that of the upwind, and also the altitude level of the strong updraft is lower than that of the upwind. The convergence of the monsoon-related southwesterly inflow and outflow from inside the stratiform rainband is the main reason for the updraft in the downwind of stratiform, which develops the enhanced reflectivity line.

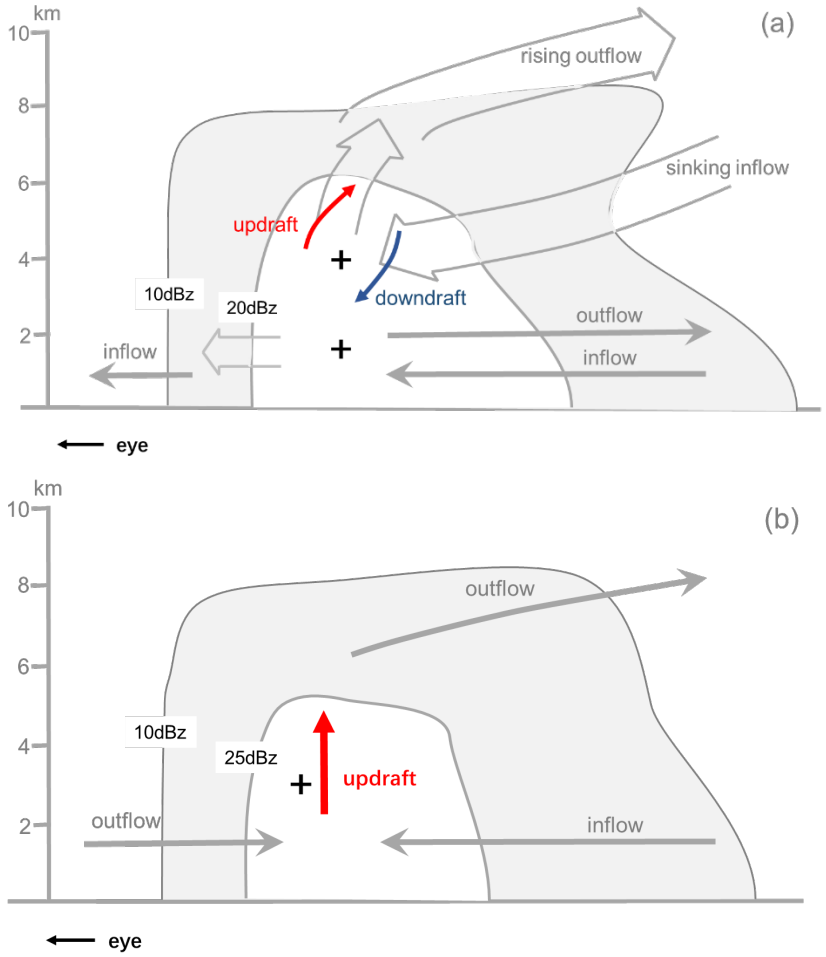

Figure 15. Schematic of the dynamics within the stratiform of outer rainband in Typhoon Higos, (**a**) the upwind of stratiform, (**b**) the downwind of stratiform. The broad arrows represent mesoscale secondary circulation. The gray line arrows represent vortex-scale motion associated with the overall storm. Red arrows mean updraft of vertical velocity. Blue arrow means downdraft of vertical velocity. Reflectivity contours are drawn. The plus signs indicate regions of increasing tangential velocity.

The intensity of Typhoon Higos is not very strong, but during the developing process of the stratiform sector of the outer rainband, the dynamic characteristics of the upwind of

the stratiform rainband are consistent with scholars' understanding of the dynamic features in the process of forming concentric eyewalls of strong typhoons. However, the dynamic characteristics of the downwind of the stratiform rainband of Typhoon Higos are distinct from those recognized by scholars, which may be associated with the weak intensity of Typhoon Higos. To recognize the dynamic characteristics of the downwind of the stratiform rainband, it is necessary to perform more typhoon case studies or thermodynamic research through numerical simulation in the future.

Author Contributions: Conceptualization, methodology, investigation and resources, R.L. (Ruiyi Li) and Q.L.; Validation and formal analysis, M.W. and R.L. (Ruifeng Li); methodology, S.W.; writing—review and editing, H.L. and L.W. All authors have read and agreed to the published version of the manuscript.

Funding: This research was funded by the National Key Research and Development Plan of China, Grant No. 2022YFC3004100.

Data Availability Statement: Not applicable.

Acknowledgments: The authors would like to thank Bobby Jackson et al. for developing the PyDDA software and Jonathan J. Helmus et al. for researching the pyart software and releasing them freely on the GitHub website.

Conflicts of Interest: The authors declare no conflict of interest.

References

1. Wang, Y. Vortex Rossby waves in a numerically simulated tropical *cyclone.* Part II: The role in tropical cyclone structure and intensity changes. *J. Atmos. Sci.* **2002**, *59*, 1239–1262. [CrossRef]
2. Skwira, G.D.; Schroeder, J.L.; Peterson, R.E. Surface observations of landfalling hurricane rainbands. *Mon. Weather Rev.* **2005**, *133*, 454–465. [CrossRef]
3. Wang, Y.; Wu, C.-C. Current understanding of tropical cyclone structure and intensity changes-A review. *Meteorol. Atmos. Phys.* **2004**, *87*, 257–278. [CrossRef]
4. Qiu, X.; Tan, Z.-M. The roles of asymmetric inflow forcing induced by outer rainbands in tropical cyclone secondary eyewall formation. *J. Atmos. Sci.* **2013**, *70*, 953–974. [CrossRef]
5. Marks, F.D.; Shay, L.K. Landfalling tropical cyclones: Forecast problems and associated research opportunities. *Bull. Amer. Meteor. Soc.* **1998**, *79*, 305–323.
6. Duan, Y. Monitoring and forecasting of finescale structure and impact assessment of landfalling typhoons. *Adv. Earth Sci.* **2015**, *30*, 847–854. [CrossRef]
7. Willoughby, H.E.; Marks, F.; Feinberg, R.J. Stationary and moving convective bands in hurricanes. *J. Atmos. Sci.* **1984**, *41*, 3189–3211. [CrossRef]
8. Atlas, D.; Hardy, K.R.; Wexler, R.; Boucher, R. On the origin of hurricane spiral bands. *Geofis. Int.* **1963**, *3*, 123–132. [CrossRef]
9. Barnes, G.M.; Zipser, E.J.; Jorgensen, D.; Marks, F., Jr. Mesoscale and convective structure of a hurricane rainband. *J. Atmos. Sci.* **1983**, *40*, 2125–2137. [CrossRef]
10. Hence, D.A.; Houze, R.A., Jr. Kinematic structure of convective-scale elements in the rainbands of Hurricanes Katrina and Rita (2005). *J. Geophys. Res.* **2008**, *113*, D15108. [CrossRef]
11. Willoughby, H.E. The dynamics of the tropical cyclone core. *Aust. Meteorol. Mag.* **1988**, *36*, 183–191.
12. Houze, R.A., Jr. Clouds in Tropical Cyclones. *Mon. Weather Rev.* **2010**, *138*, 293–344. [CrossRef]
13. Black, R.A.; Hallett, J. Observations of the distribution of ice in hurricanes. *J. Atmos. Sci.* **1986**, *43*, 802–822. [CrossRef]
14. Molinari, J.; Moore, P.; Idone, V. Convective structure of hurricanes as revealed by lightning locations. *Mon. Weather Rev.* **1999**, *127*, 520–534. [CrossRef]
15. Powell, M.D. Boundary layer structure and dynamics in outer hurricane rainbands. Part I: Mesoscale rainfall and kinematic structure. *Mon. Weather Rev.* **1990**, *118*, 891–917. [CrossRef]
16. Powell, M.D. Boundary layer structure and dynamics in outer hurricane rainbands. Part II: Downdraft modification and mixed layer recovery. *Mon. Weather Rev.* **1990**, *118*, 918–938. [CrossRef]
17. Franklin, C.N.; Holland, G.J.; May, P.T. Mechanisms for the generation of mesoscale vorticity features in tropical cyclone rainbands. *Mon. Weather Rev.* **2006**, *134*, 2649–2669. [CrossRef]
18. Didlake, A.C., Jr.; Houze, R.A., Jr. Convective-scale downdrafts in the principal rainband of Hurricane Katrina (2005). *Mon. Weather Rev.* **2009**, *137*, 3269–3293. [CrossRef]
19. Didlake, A.C., Jr.; Houze, R.A., Jr. Dynamics of the stratiform sector of a tropical cyclone rainband. *J. Atmos. Sci.* **2013**, *70*, 1891–1911. [CrossRef]

20. Didlake, A.C., Jr.; Reasor, P.D.; Rorgers, R.F.; Lee, W.C. Dynamics of the Transition from Spiral Rainbands to a Secondary Eyewall in Hurricane Earl (2010). *J. Atmos. Sci.* **2018**, *75*, 2909–2929. [CrossRef]
21. Cha, T.Y.; Bell, M.M.; Lee, W.C.; DesRosiers, A.J. Polygonal Eyewall Asymmetries During the Rapid Intensification of Hurricane Michael(2018). *Geophys. Res. Lett.* **2020**, *47*, e2020GL087919. [CrossRef]
22. Lee, W.-C.; Jou, B.J.-D.; Chang, P.-L.; Deng, S.-M. Tropical cyclone kinematic structure retrieved from single-Doppler radar observations. Part I: Interpretation of Doppler velocity patterns and the GBVTD technique. *Mon. Weather Rev.* **1999**, *127*, 2419–2439. [CrossRef]
23. Jou, B.J.-D.; Lee, W.-C.; Liu, S.-P.; Kao, Y.-C. Generalized VTD retrieval of atmospheric vortex kinematic structure. Part I: Formulation and error analysis. *Mon. Weather Rev.* **2008**, *136*, 995–1012. [CrossRef]
24. Cha, T.Y.; Bell, M.M. Comparison of Single Doppler and Multiple Doppler Wind Retrievals in Hurricane Matthew (2016). *Atmos. Meas. Tech.* **2021**, *14*, 3523–3539. [CrossRef]
25. Zhou, S.; Wei, M.; Zhang, P.; Xu, H.; Zhao, C. The precipitation particles'vertical velocity retrieval with single Doppler weather radar. Part I: Retrieval method's analysis. *Acta Meteorol. Sin.* **2014**, *72*, 760–771. [CrossRef]
26. Zhou, S.; Wei, M.; Zhang, P.; Xu, H.; Zhang, M. The precipitation particles'vertical velocity retrieval with single Doppler weather radar. Part II: Case analysis. *Acta Meteorol. Sin.* **2014**, *72*, 772–781. [CrossRef]
27. Black, M.L.; Gamache, J.F.; Marks, F.D.; Samsury, C.E.; Willoughby, H.E. Eastern Pacific Hurricanes Jimena of 1991 and Olivia of 1994: The effect of vertical shear on structure and intensity. *Mon. Weather Rev.* **2002**, *130*, 2291–2312. [CrossRef]
28. Reasor, P.D.; Rogers, R.; Lorsolo, S. Environmental flow impacts on tropical cyclone structure diagnosed from airborne Doppler radar composites. *Mon. Weather Rev.* **2013**, *141*, 2949–2969. [CrossRef]
29. DeHart, J.C.; Houze, R.A.; Rogers, R.F. Quadrant distribution of tropical cyclone inner-core Kinematics in relation to environmental shear. *J. Atmos. Sci.* **2014**, *71*, 2713–2732. [CrossRef]
30. Potvin, C.K.; Betten, D.; Wicker, L.J.; Elmore, K.L.; Biggerstaff, M.I. 3DVAR versus traditional dual-Doppler wind retrievals of a simulated supercell thunderstorm. *Mon. Weather Rev.* **2012**, *140*, 3487–3494. [CrossRef]
31. Potvin, C.K.; Wicker, L.J.; Shapiro, A. Assessing errors in variational dual-Doppler wind syntheses of supercell thunderstorms observed by storm-scale mobile radars. *J. Atmos. Ocean. Technol.* **2012**, *29*, 1009–1025. [CrossRef]
32. Oue, M.; Kollias, P.; Sharpiro, A.; Tatarevic, A.; Matsui, T. Investigation of observational error sources in multi-Doppler-radar three-dimensional variational vertical air motion retrievals. *Atmos. Meas. Tech.* **2019**, *12*, 1999–2018. [CrossRef]
33. Tatarevic, A.; Kollias, P.; Oue, M.; Wang, D.; Yu, K. User's Guide CR-SIM SOFTWARE v 3.1, Brookhaven National Laboratory–Stony Brook University McGill University Radar Science Group. Available online: https://you.stonybrook.edu/radar/research/radar-simulators/ (accessed on 19 June 2020).
34. Hong, S.Y.; Lim, J.O.J. The WRF single-moment 6-class microphysics scheme (WSM6). *J. Korean Meteor. Soc.* **2006**, *42*, 129–151.
35. Lee, J.D.; Wu, C.C. The role of polygonal eyewalls in rapid intensification of typhoon Megi (2010). *J. Atmos. Sci.* **2018**, *75*, 4175–4199. [CrossRef]
36. Qin, N.N.; Zhang, D.L.; Miller, W.; Kieu, C.Q. On the rapid intensification of Hurricane Wilma (2005). Part IV: Inner-core dynamics during the steady radius of maximum wind stage. *Quart. J. Roy. Meteor. Soc.* **2018**, *144*, 2508–2523. [CrossRef]
37. Pang, Q.Y.; Ping, F.; Shen, X.Y.; Liu, L.K. A comparative study of effects of different microphysics schemes on precipitation simulation for typhoon Mujigae (2015). *Chinese J. Atmos. Sci.* **2019**, *43*, 202–220. [CrossRef]
38. Zhang, P.; He, P.; Song, C.; Ge, R. A study on error distribution and radar optimum arrangements of wind field measurement with Doppler radars. *Acta Meteorol. Sin.* **1998**, *1*, 96–103. [CrossRef]

Disclaimer/Publisher's Note: The statements, opinions and data contained in all publications are solely those of the individual author(s) and contributor(s) and not of MDPI and/or the editor(s). MDPI and/or the editor(s) disclaim responsibility for any injury to people or property resulting from any ideas, methods, instructions or products referred to in the content.